# *In vivo* two-photon microscopy reveals the contribution of Sox9$^+$ cell to kidney regeneration in a mouse model with extracellular vesicle treatment

Received for publication, January 20, 2020, and in revised form, July 2, 2020 Published, Papers in Press, July 8, 2020, DOI 10.1074/jbc.RA120.012732

**Kaiyue Zhang[1,2,‡], Shang Chen[1,2,‡], Huimin Sun[1], Lina Wang[3], Huifang Li[1], Jinglei Zhao[1], Chuyue Zhang[4], Nana Li[5], Zhikun Guo[5], Zhibo Han[6,7], Zhong-Chao Han[6,7,8], Guoguang Zheng[3,*], Xiangmei Chen[4,*], and Zongjin Li[1,2,4,5,*]**

*From the [1]Nankai University School of Medicine, Tianjin, China, [2]The Key Laboratory of Bioactive Materials, Ministry of Education, the College of Life Sciences, Nankai University, Tianjin, China, [3]State Key Laboratory of Experimental Hematology, National Clinical Research Center for Blood Diseases, Institute of Hematology and Blood Diseases Hospital, Chinese Academy of Medical Sciences and Peking Union Medical College, Tianjin, China, [4]State Key Laboratory of Kidney Diseases, Chinese PLA General Hospital, Beijing, China, [5]Henan Key Laboratory of Medical Tissue Regeneration, Xinxiang Medical University, Xinxiang, China, [6]Jiangxi Engineering Research Center for Stem Cell, Shangrao, Jiangxi, China, [7]Tianjin Key Laboratory of Engineering Technologies for Cell Pharmaceutical, National Engineering Research Center of Cell Products, AmCellGene Co., Ltd., Tianjin, China, and [8]Beijing Engineering Laboratory of Perinatal Stem Cells, Beijing Institute of Health and Stem Cells, Health & Biotech Co., Beijing, China*

Edited by Mike Shipston

**Mesenchymal stem cell (MSC)–derived extracellular vesicles (EVs) have been shown to stimulate regeneration in the treatment of kidney injury. Renal regeneration is also thought to be stimulated by the activation of Sox9$^+$ cells. However, whether and how the activation mechanisms underlying EV treatment and Sox9$^+$ cell–dependent regeneration intersect is unclear. We reasoned that a high-resolution imaging platform in living animals could help to untangle this system. To test this idea, we first applied EVs derived from human placenta–derived MSCs (hP-MSCs) to a Sox9-Cre$^{ERT2}$; R26$^{mTmG}$ transgenic mouse model of acute kidney injury (AKI). Then, we developed an abdominal imaging window in the mouse and tracked the Sox9$^+$ cells in the inducible Sox9-Cre transgenic mice via *in vivo* lineage tracing with two-photon intravital microscopy. Our results demonstrated that EVs can travel to the injured kidneys post intravenous injection as visualized by Gaussia luciferase imaging and markedly increase the activation of Sox9$^+$ cells. Moreover, the two-photon living imaging of lineage-labeled Sox9$^+$ cells showed that the EVs promoted the expansion of Sox9$^+$ cells in kidneys post AKI. Histological staining results confirmed that the descendants of Sox9$^+$ cells contributed to nephric tubule regeneration which significantly ameliorated the renal function after AKI. In summary, intravital lineage tracing with two-photon microscopy through an embedded abdominal imaging window provides a practical strategy to investigate the beneficial functions and to clarify the mechanisms of regenerative therapies in AKI.**

Despite an increasing incidence of acute kidney injuries (AKI) across the globe and poor prognosis of the survivors, including chronic kidney disease, end-stage renal disease, and ultimately death, only a few preventive and therapeutic treatments exist (1, 2). With growing insight into the causes and mechanisms of AKI, sex-determining region Y box 9 (Sox9) has been demonstrated to play a pivotal role in renal regeneration in AKI (3, 4). Sox9 was found to be expressed in the proximal tubule cells, starting at an early stage (within 24 h) post AKI (3, 4). Moreover, the Sox9-positive (Sox9$^+$) cells were thought to be the progenitor-like cells which possessed high proliferative capacity and were the major contributors to kidney regeneration after AKI (4). To date, however, the effective therapeutic strategy to promote the endogenous Sox9$^+$ cells activation for AKI treatment was little reported.

Extracellular vesicles (EVs) are considered a kind of intercellular communication vehicle with the ability to transport informational molecules in the form of nucleic acids, proteins, and lipids (5–9). EVs derived from mesenchymal stem cells (MSCs) that contain the functional compositions from MSCs have been widely employed in tissue repair and regenerative medicine (8, 10–13). Recent studies have reported that MSC-derived EVs could attenuate renal injury and improve renal outcomes in a series of experimental AKI models (14–16). Besides, the possible therapeutic mechanism of MSC-derived EVs for AKI treatment was related to the Sox9 expression (17). Unfortunately, there is still no real-time monitoring method or precise assessment measure for Sox9$^+$ cells activation and renal repair, which severely limits the research and application of MSC-derived EVs in AKI treatment.

Lineage tracing is recently being used as a powerful tool in tissue regeneration and stem cell research by labeling a specific type of cells, which offers an opportunity to visualize the cell behavior in the context of the intact organism instead of the *in vitro* environment (18–20). The research based on the lineage tracing of Sox9$^+$ cell mouse models provides novel insight into the Sox9$^+$ cells in renal development, the cell fate during renal injury, and the potential mechanisms of renal regeneration (3, 4, 21). However, the conventional research method of lineage tracing relying on sacrificing the animals to get the information on the tissue sections is only a "snapshot" (19, 22), which is

This article contains supporting information.
‡These authors contributed equally to this work.
*For correspondence: Zongjin Li, zongjinli@nankai.edu.cn; Xiangmei Chen, xmchen301@126.com; Guoguang Zheng, zhengggtjchn@aliyun.com.

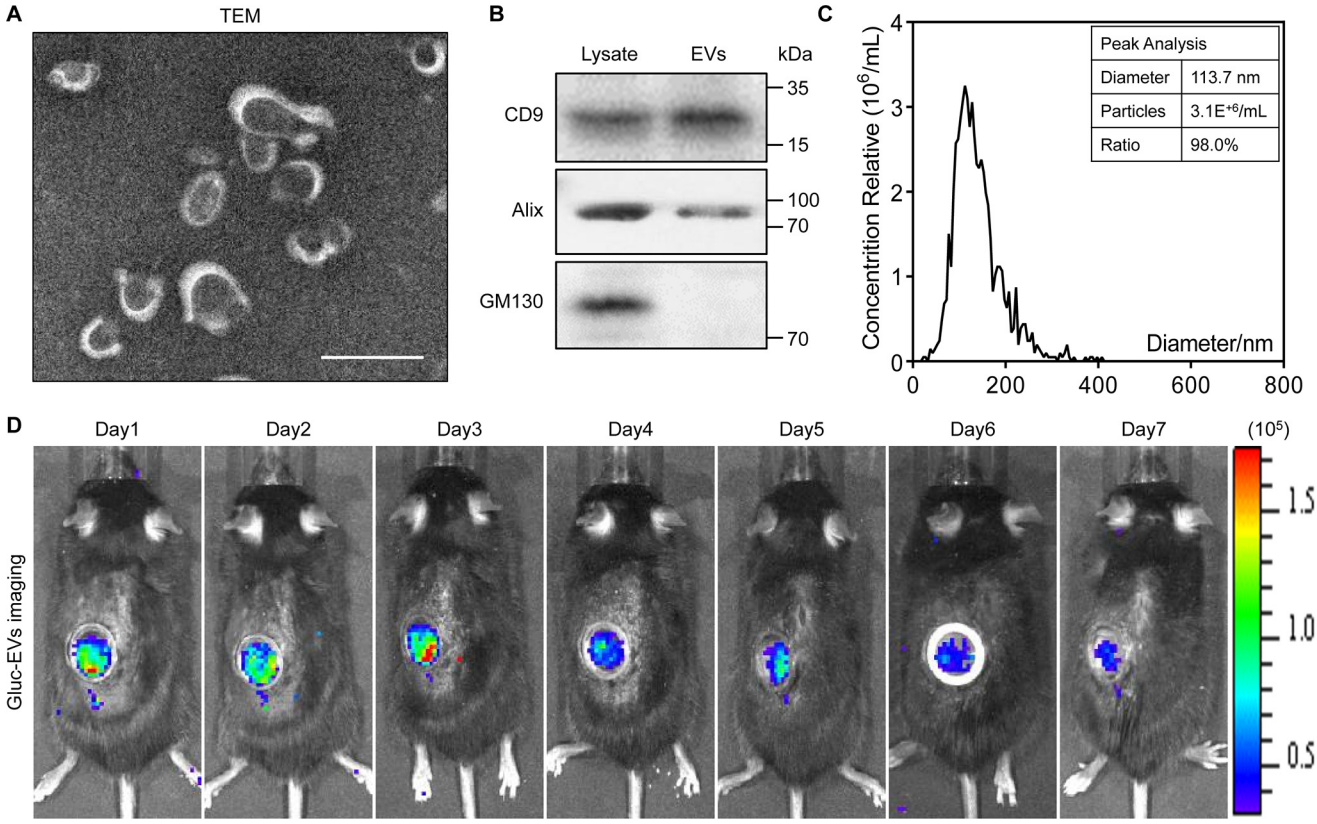


**Figure 1. Characteristics and bioluminescence imaging of EVs.** *A*, transmission electron microscope (*TEM*) image of EVs. *Scale bar*, 100 nm. *B*, Western blot analysis confirmed the three categories of exosomal markers: CD9, Alix, and GM130. *C*, nanoparticle tracking analysis indicates the peak diameter of EVs is 113.7 nm. *D*, the biodistribution of EVs was traced *in vivo* by Gaussia luciferase (Gluc) imaging through the AIW.

unable to dynamically monitor the Sox9$^+$ cell behavior in action. The abdominal imaging window (AIW) successfully solves this problem, making researchers able to visualize as well as quantify the cell fate and reparative process by lineage tracing in real-time, *in vivo* in an individual mouse (23–25). In addition, the application of two-photon microscopy (TPM) improves the feasibility of lineage tracing by living imaging at a single-cell level because of its advantages, such as deep tissue penetration and little photodamage (22).

In this study, we used high-resolution intravital *in situ* imaging techniques to examine the kinetics of Sox9$^+$ cells in mouse AKI under the treatment of human placental MSCs (hP-MSCs)–derived EVs. We utilized an inducible Sox9-Cre transgenic mice with AIW to evaluate the influence of EVs on Sox9 expression at a single-cell level and further assess the therapeutic effect of EVs for AKI. The Sox9$^+$ cell–dependent repair process in injured kidney was observed in real-time by TPM living imaging. Our data suggested that EVs promoted the Sox9$^+$ cell proliferation and further accelerated the renal regeneration via the activation of Sox9$^+$ cells.

## Results

### *Characteristics and biodistribution of EVs*

The transmission electron microscope image showed that the morphology of EVs was membrane-bound round-shaped vesicles (Fig. 1*A*). Three categories of protein markers were confirmed by Western blot analysis. The bands of the EVs and donor cells demonstrated that the EVs we collected contained the exosomal markers CD9 and Alix and excluded the protein GM130, which is expressed in the Golgi complex (Fig. 1*B*). The result of nanoparticle tracking analysis revealed that the diameter of the EVs was ~110 nm (Fig. 1*C*).

To trace the biodistribution of EVs in renal IRI mice after intravenous injection, we utilized a bioluminescence report system to label EVs as described previously (Fig. S1, *A* and *B*) (26). The hP-MSCs were transduced with the lentivirus that carried the gene sequence of Gluc-lactadherin fusion protein. As a consequence, the membrane of EVs released from the transduced hP-MSCs gathered the Gluc-lactadherin fusion protein, which means the EVs were labeled by Gluc. After the IRI, we intravenously injected Gluc-labeled EVs at a dose of 100 $\mu$g in a volume of 100 $\mu$l for 3 consecutive days. To avoid the blocking from the skin and abdominal wall, we implanted an AIW in the kidney region of the abdomen. The BLI images exhibited that robust signals were emitted from the kidney region through the AIW in the first 3 days and faded in subsequent days, which indicated the successful arrival of EVs at the injured kidney after intravenous injections (Fig. 1*D*). In summary, the EVs that were isolated from the conditional medium of hP-MSCs could arrive at the injured kidney and be used in the AKI treatment.

### *EVs inhibited cell apoptosis*

To investigate the therapeutic effects of EVs, it is necessary to observe in real-time the bioprocesses in the injured kidneys

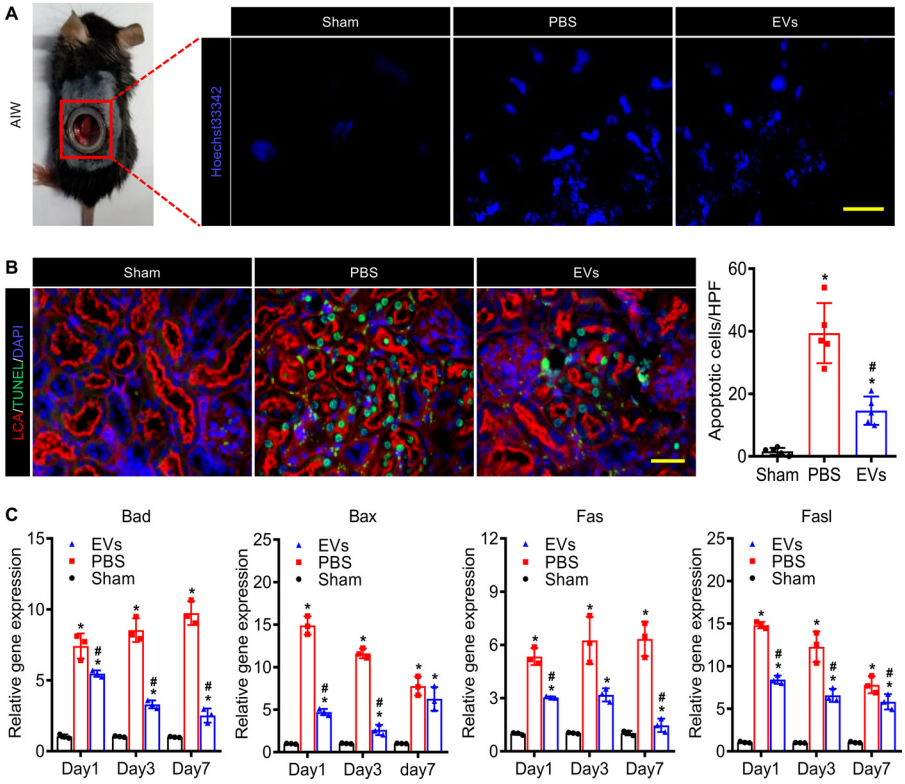


**Figure 2. EVs suppressed apoptosis of the kidney after ischemia-reperfusion injury.** *A*, fluorescence stereomicroscope imaging of the injured kidney stained by Hoechst 33342 through the embedded AIW. *Scale bar*, 100 $\mu$M. *B*, the TUNEL staining (*green*) of the kidney sections (rhodamine-labeled LCA, *red*, proximal tubular) on day 3. *Scale bar*, 50 $\mu$M. *C*, real-time qPCR analysis of apoptosis-related genes in injured kidneys on days 1, 3, and 7 after IRI. Relative gene expression was normalized to *Gapdh*. The experiments were performed in triplicate. Data are expressed as scatter plots with mean ± S.D. *, $P < 0.05$ *versus* Sham; #, $P < 0.05$ *versus* PBS.

*in vivo* dynamically. The AIWs in renal IRI mice were useful for freely and directly observing the injured kidneys and performing fluorescence imaging of renal tissues for an extended period of time. Hoechst 33342, a bis-benzamide derivative that binds specifically to DNA, could be utilized to trace the apoptosis cells. Therefore, we intravenously injected 10 mg/kg Hoechst 33342 into renal IRI mice to evaluate the states of injured kidneys by using the fluorescence stereomicroscope. The images of intravital Hoechst 33342 imaging revealed that EVs ameliorated the IRI-induced apoptosis of the injured kidney (Fig. 2*A*). In addition, we assessed the renal cell apoptosis in tissue sections on day 3 post IRI by TUNEL assay. As the data show, IRI resulted in massive tubule epithelial cells (TECs) death and EVs alleviated TEC apoptosis compared with PBS (Fig. 2*B*). Moreover, the real-time qPCR analysis (Table S1) of the renal tissues in each group showed that EVs significantly inhibited the TEC apoptosis via suppressing apoptosis-related genes (Fig. 2*C* and Fig. S2). These results indicated that EVs remarkably ameliorated the IRI induced TECs apoptosis in AKI treatment.

### *EVs activated Sox9 expression*

The kidneys, to an extent, have some ability to regenerate after an acute injury, which appeared as a significant regenerative response characterized by cell proliferation. Therefore, we detected the cell proliferation in EVs treated kidney on day 3 post IRI by proliferating cell nuclear antigen (PCNA) immunostaining. Cells were largely quiescent in normal kidney, but IRI invoked a discernible proliferative response 3 days post injury. In addition, PCNA$^+$ cells in the EV-treated kidney markedly increased compared with the ones administrated with PBS (Fig. 3*A*). The anti-Sox9 immunostaining studies confirmed that injury stimulated Sox9 expression and EVs significantly increased the protein expression of Sox9 on day 3 after IRI (Fig. 3*B*). We found that Sox9 was mainly expressed in proximal tubule epithelial cells with evident epithelial polarity, an apical and LTL-enriched brush border. Therefore, we used the HK2 cells to further investigate the proliferation promotion effect of EVs. After incubating DiI-labeled EVs with HK2 cells for 6 h, we observed the EVs were internalized by HK2 cells (Fig. S3*A*). Moreover, the cell proliferation assay indicated that the EVs stimulated the HK2 cell proliferation in a dose-dependent manner with a peak of 50 $\mu$g/ml (Fig. S3*B*). Meanwhile, we performed the immunostaining of anti-Sox9 and anti-Ki67 to the HK2 cells which were incubated with EVs for 24 h. The EVs remarkably activated the expression of Sox9 and Ki67 in HK2 cells (Fig. 3*C*). The Western blotting analysis also revealed that the EVs promoted the expression of Sox9 in HK2 cells (Fig. 3*D*). All these data suggested that the administration of EVs stimulated the Sox9 expression in renal tubule epithelial cells after AKI.

### *Two-photon living imaging of Sox9$^+$ cells*

To determine whether EV-induced Sox9$^+$ cells actively contribute to renal regeneration, we performed intravital

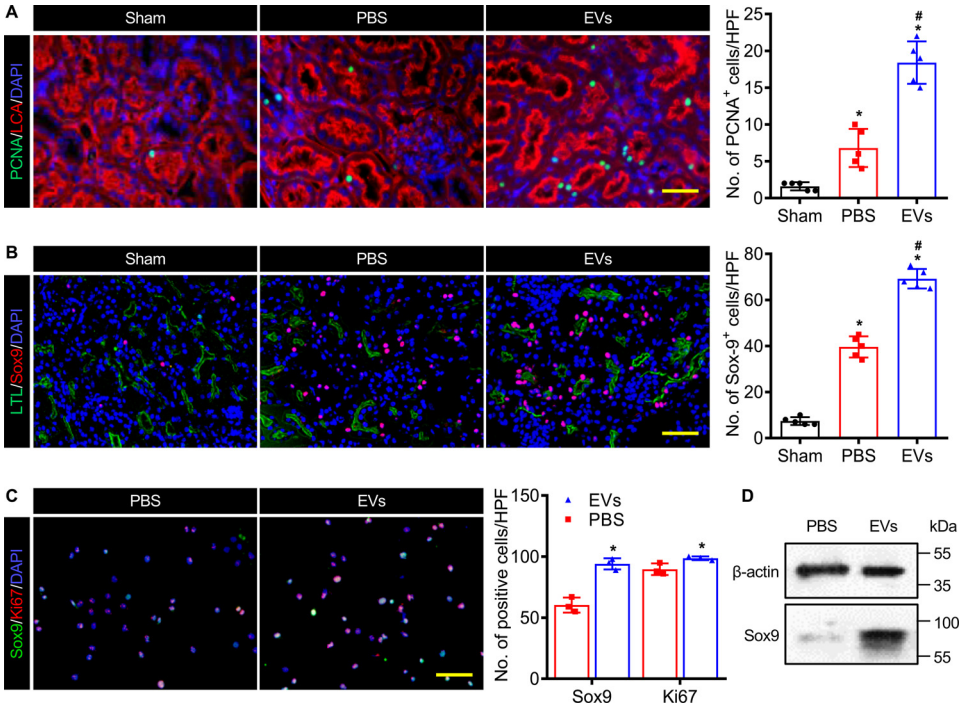


**Figure 3. EVs improved the Sox9 activation in the injured kidney.** *A*, anti-PCNA immunostaining (*green*) of proximal tubules (rhodamine-labeled LCA, *red*) on day 3 post IRI. *Scale bar*, 50 $\mu$M. *B*, representative images and analysis of anti-Sox9 immunostaining (*red*) in kidney (FITC-labeled LTL, *green*, proximal tubules) at 3 days after IRI. *Scale bar*, 100 $\mu$M. *C*, immunostaining analysis for Sox9 (*green*) and Ki67 (*red*) in HK2 cells treated with EVs for 24 h. *Scale bar*, 100 $\mu$M. DAPI demarcates nuclei. *D*, Western blot analysis of Sox9 expression in HK2 cells treated with EVs for 24 h. Data are expressed as scatter plots with mean ± S.D. *, $P < 0.05$ *versus* Sham; #, $P < 0.05$ *versus* PBS.

lineage tracing of Sox9$^+$ cells on renal IRI mice (Fig. 4*A*). To this end, we generated a kind of tamoxifen-inducible mice named Sox9-Cre$^{ERT2}$; R26$^{mTmG}$, specifically labeling the Sox9$^+$ cells by cross-ing Sox9 promoter-driven Cre$^{ERT2}$ mice (Sox9-Cre$^{ERT2}$) to R26$^{mTmG}$ mice. In this mice, intraperitoneal injection of tamoxifen resulted in efficient labeling Sox9$^+$ cells and their descendants with membrane-localized EGFP, while other cells were marked with membrane-localized tdTomato (Fig. 4*B*). To validate the mouse genetic model, we inspected the Sox9$^+$ cells and EGFP fluorescence co-location in kidney after three consecutive tamoxifen injection (corn oil as control) before and after AKI by anti-Sox9 immunostaining. The results revealed that EGFP was only expressed in the Sox9 positive cells after tamoxifen induction and no spontaneous AKI-induced Cre activation in Sox9-Cre$^{ERT2}$; R26$^{mTmG}$ mice (Fig. S4).

Then, we utilized the AIW again to implement intravital imaging of Sox9$^+$ cells using two-photon microscope. In the sham operation group, the substantially all renal cells were tdTomato$^+$, indicating that renal cells were largely Sox9 negative (Sox9$^-$) in normal adult kidney (Fig. 4*C*). Meanwhile, we observed an expansion of Sox9$^+$ cells (displayed EGFP fluorescence) in kidney after injury (Fig. 4*C*), which were consistent with literature reported (3, 4). Interestingly, compared with PBS group, we found EVs significantly increased the number of the EGFP$^+$ cells, suggesting the EVs helped the injured kidney replenished with abundant expanded clusters of Sox9$^+$ cells (Fig. 4, *C* and *D*). According to the lineage tracing, we demonstrated the bulk of cells that repaired injury kidney derived from the Sox9$^+$ cells, and the EVs further activated this process.

### *Increased nephric tubule regeneration by EVs*

To observe the process of EVs promoted recovery, the two-photon living imaging and 3D reconstruction technique were used to track lineage-labeled EGFP$^+$ cells and renal structures in Sox9-Cre$^{ERT2}$; R26$^{mTmG}$ mice. We identified the functional renal tubules were formed by the descendants of Sox9$^+$ cells on days 1, 3, 7, and 14 post IRI with EV treatment and observed their detailed tubular morphologies in X, Y, and *z* axis with high resolution (Fig. 5*A* and Videos S1–S4). Taking advantage of the clarity of the AIW, we conducted two-photon imaging up to a depth of 100 $\mu$M and visualized the renal structures. To confirm our two-photon imaging data, the EGFP$^+$ cells and renal structures in the EVs treated kidneys were evaluated by immunostaining on day 14 after injury. In these three groups, the newly formed EGFP$^+$ cells were all E-cadherin$^+$, which indicated that the re-formation of functional renal tubules was mainly attributed to the proliferation of pre-existing Sox9$^+$ cells in injured kidneys (Fig. 5*B* and Fig. S5*A*). Furthermore, we found the renal tubules composed entirely of EGFP$^+$ cells only existed in the EVs treated kidney (Fig. 5*C* and Fig. S5, *B* and *C*). Taken together, descendants of Sox9$^+$ cells regenerate the majority of injured renal tubules after IRI-induced reactivation of Sox9 and this regenerative ability of Sox9$^+$ cells was significantly accelerated by EV treatment.

### *EVs activated Sox9 expression and Sox9$^+$ cells proliferation*

To obtain a better sense of the relationship between the EVs and Sox9 activity during renal regeneration, we performed an anti-Sox9 immunostaining analysis of the kidney samples

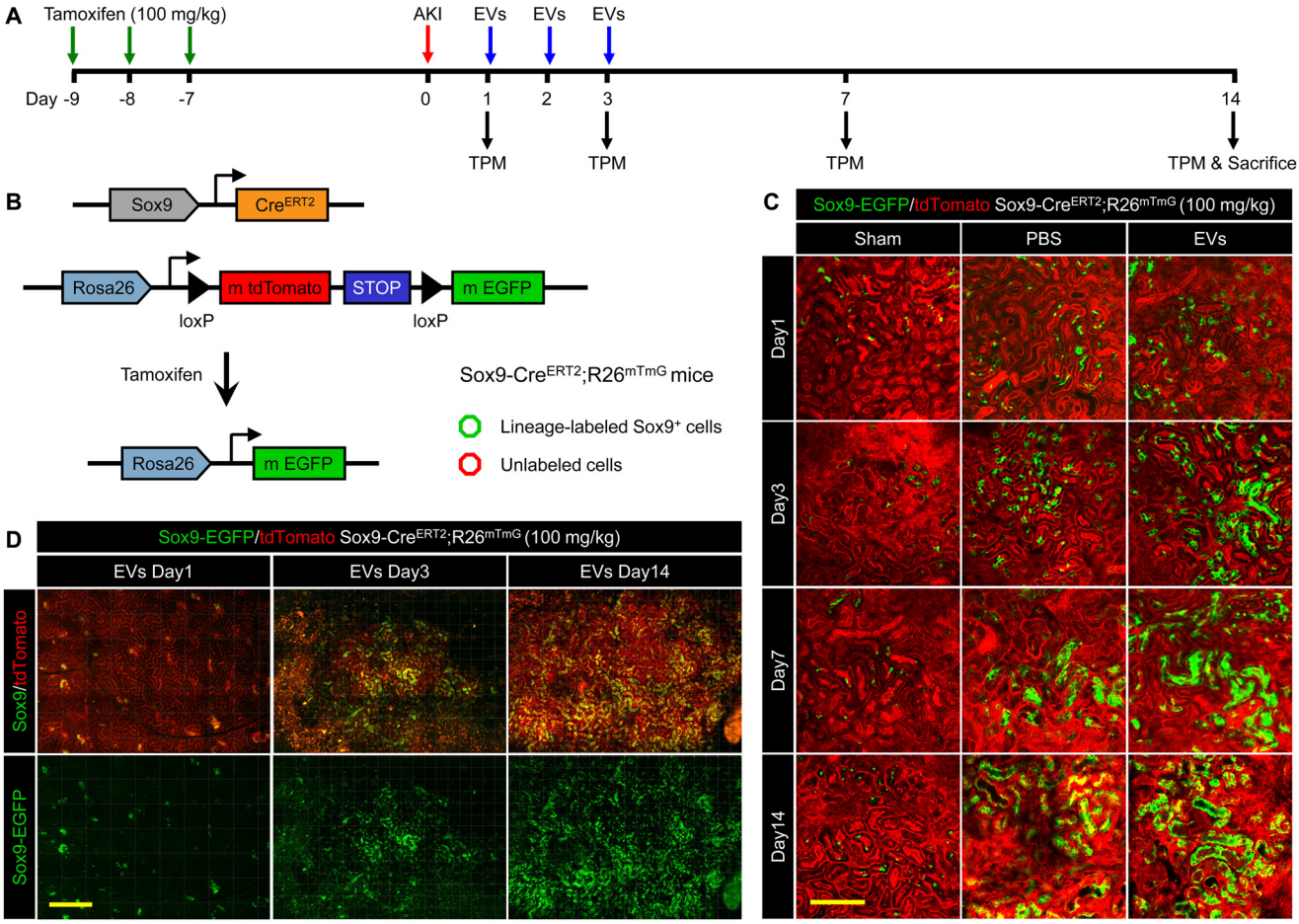


**Figure 4. Two-photon living imaging of Sox9$^+$ cells expansion following EV treatment.** *A*, schematic illustration for two-photon living imaging of lineage tracing marked Sox9$^+$ cells after renal IRI and EV treatment. Sox9-Cre$^{ERT2}$; R26$^{mTmG}$ mice were injected intraperitoneally with tamoxifen once a day for 3 continuous days to label the Sox9$^+$ cells. 7 days after the final tamoxifen injection, the renal ischemia-reperfusion injury was performed in these mice with simultaneous implantation of AIW. The EVs or PBS were intravenously injected once a day for 3 continuous days post IRI. The two-photon living imaging was carried out on days 1, 3, 7, and 14 after IRI. The kidney tissues were collected on day 14 after the injury. *B*, the scheme of generation of a tamoxifen-inducible Sox9-Cre$^{ERT2}$; R26$^{mTmG}$ mice for genetic lineage tracing. *C*, the representative images of two-photon intravital tracing showed Sox9$^+$ cell-derived cells abundantly expanded with the administration of EVs. *Scale bar*, 200 $\mu$M. *D*, whole-vision scans of the injured kidney from the same mouse treated with EVs through the embedded AIW by using a two-photon microscope on days 1, 3, and 14 post IRI. *Scale bars*, 500 $\mu$M.

collected from Sox9-Cre$^{ERT2}$; R26$^{mTmG}$ mice on day 14 after the last two-photon imaging. In the normal adult kidneys, there were only rare EGFP$^+$ cells, mostly Sox9$^-$. This suggested that only a small number of renal cells were renewed from Sox9$^+$ cells and then lost their Sox9$^+$ characteristics (appeared as Sox9$^-$) in the physiological situation. Post IRI, the injury stimulated the expansion of EGFP$^+$ cells as well as emerged the Sox9 expression, but most descendants of EGFP$^+$ cells no longer expressed the Sox9 gene. It was intriguing that EVs not only promoted the expansion of EGFP$^+$ cells but also maintained their expression of Sox9 for a period of time (Fig. 6, *A* and *B*, and Fig. S6). These data indicated that EVs could wake the Sox9 emergence and promote the expansion of the EGFP$^+$ cells following maintaining their progenitor-like cell characteristics. In addition, the immunostaining of anti-Ki67 showed similar results, which may be the result of a possible correlation with the Sox9 expression. After IRI, the Ki67 was expressed in a part of TECs activated by the injury. Administration of EVs notably increased the number of Ki67$^+$ cells compared with the PBS group. Besides, the newly formed EGFP$^+$ cells almost did not express the Ki67 proteins in normal or injured kidneys, while the newly formed EGFP$^+$ cells could keep the Ki67$^+$ after treatment with the EVs (Fig. 6, *C* and *D*, and Fig. S7). These results revealed that EVs could activate the proliferation of the injured TECs and promote the expansion of the EGFP$^+$ cells following holding their proliferation capacity. Taken together, these findings indicated that the EVs promoted the expansion of EGFP$^+$ cells while maintaining their progenitor-like cell characteristics, in parallel, stimulated more cells to express Sox9 after enhancing their proliferation capacity (Fig. 6*E*).

### *EVs ameliorated renal function*

In the end, we examined the therapeutic effects of EV treatment in AKI via histological analysis and renal function analysis. Histological changes at the early stage (day 3 post IRI) were evaluated by H&E staining. The IRI caused formation of a mass of necrotic tubule accompanied by cast formation and brush border loss and this process was significantly reduced with EVs treatment (Fig. 7*A* and Fig. S8, *A* and *B*). In the meantime, immunostaining of kidney injury marker (Kim-1) revealed similar

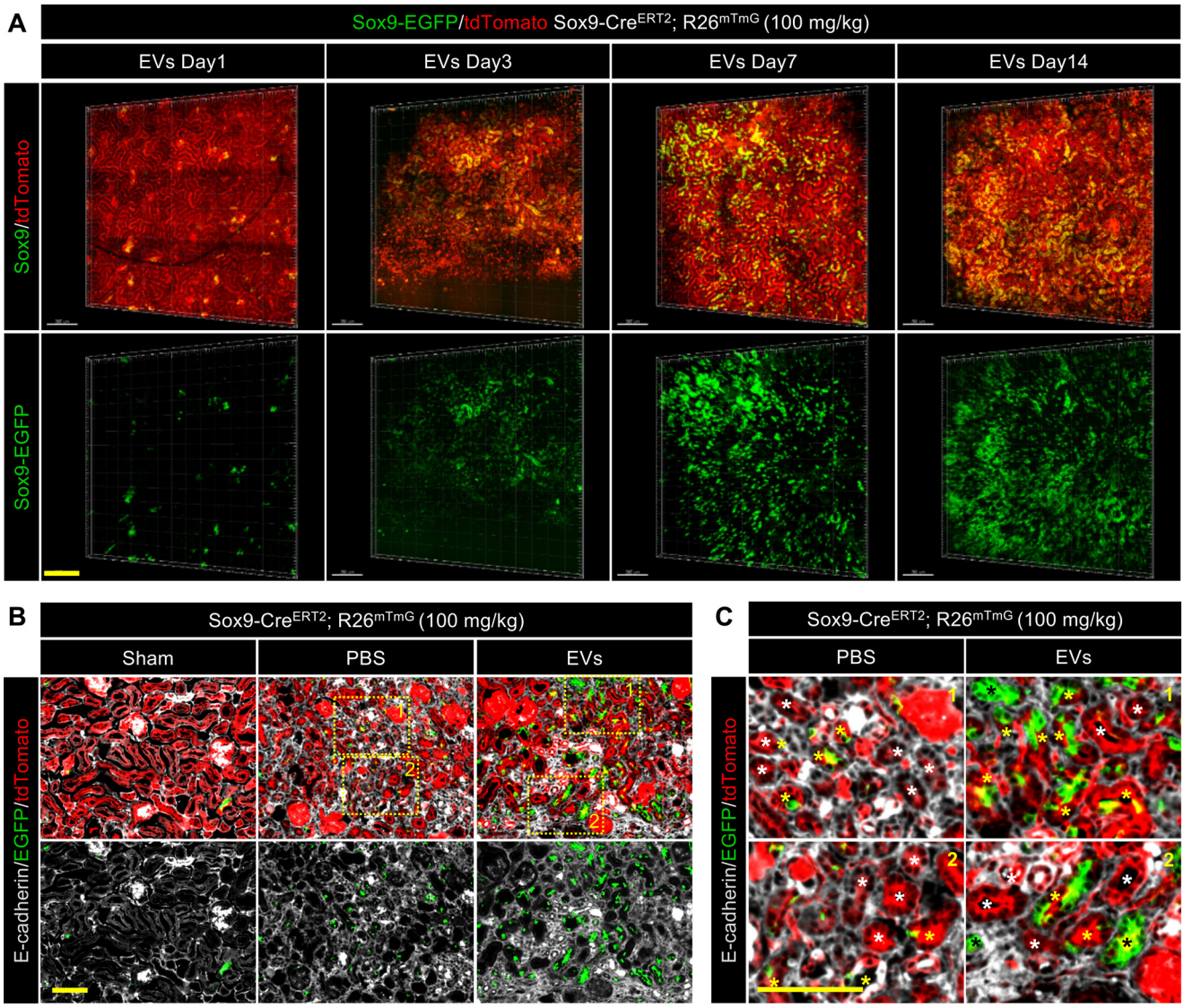


**Figure 5. EVs promoted the formation of functional renal tubules by descendants of the Sox9$^+$ cells.** *A*, 3D reconstruction of the dynamic variation in the injured kidney treated with EVs by using two-photon living imaging. *Scale bar*, 200 μM. *B* and *C*, representative images (*B*) and local zoom images (*C*) for co-localization analysis of anti-E-cadherin immunostaining (*gray*) and Sox9-Cre$^{ERT2}$–activated EGFP fluorescence in kidneys at 14 days post injury. *White asterisks* highlighted the tubules formed by descendants of Sox9$^-$ cells. *Yellow asterisks* highlighted the tubules formed by descendants of both Sox9$^+$ cells and Sox9$^-$ cells. *Black asterisks* highlighted the tubules formed by descendants of only Sox9$^+$ cells. *Scale bar*, 100 μM.

results. Compared with the PBS group, the kidney treated with EVs showed fewer Kim-1$^+$ renal tubules on day 3 post injury (Fig. 7*B* and Fig. S8*C*). After the injury, renal fibrosis usually led to progressive dysfunction of the kidney which may ultimately result in end-stage renal disease. Hence, we performed Masson staining and anti-α-SMA immunostaining to evaluate renal fibrosis on day 28 post IRI. Quantification of the fibrotic area exhibited that EVs significantly reduced the area of fibrosis (Fig. 7, *C* and *D*, and Fig. S9*A*). Anti-α-SMA immunostaining confirmed EVs could alleviate the renal fibrosis in parallel (Fig. 7, *C* and *D*, and Fig. S9*B*). Moreover, the histologic results were confirmed by real-time qPCR analysis of fibrosis-related genes. The gene expressions of fibronectin 1 (*Fn1*), collagen, type I-α1 (*ColI-α1*), and transforming growth factor-β1 (*Tgf-β1*) in kidneys were notably inhibited by EV treatment (Fig. S9*C*). The BUN and SCr were measured on days 1, 3, and 7 post injury to assess the renal function. After IRI, the concentrations of BUN and SCr were increased, which reflected the deterioration of renal function. Administration of EVs remarkably ameliorated the renal function of the injured kidney, which was manifested as the reduction in the BUN and SCr levels (Fig. 7*E*). Conclusively, EV treatment promoted kidney regeneration via amelioration of renal function and suppression of renal fibrosis.

## Discussion

In this study, our results demonstrated that intravital TPM could be used for lineage tracing Sox9$^+$ cells *in situ* through AIW at single-cell level in a mouse model of AKI. We further investigated the therapeutic effects of hP-MSC-derived EVs and verified that EVs could remarkably activate the endogenous Sox9$^+$ cells to form functional renal tubules, so as to assist restoring the damaged renal tissue. The embedded AIW provided the feasibility to intravital monitor EV distribution and

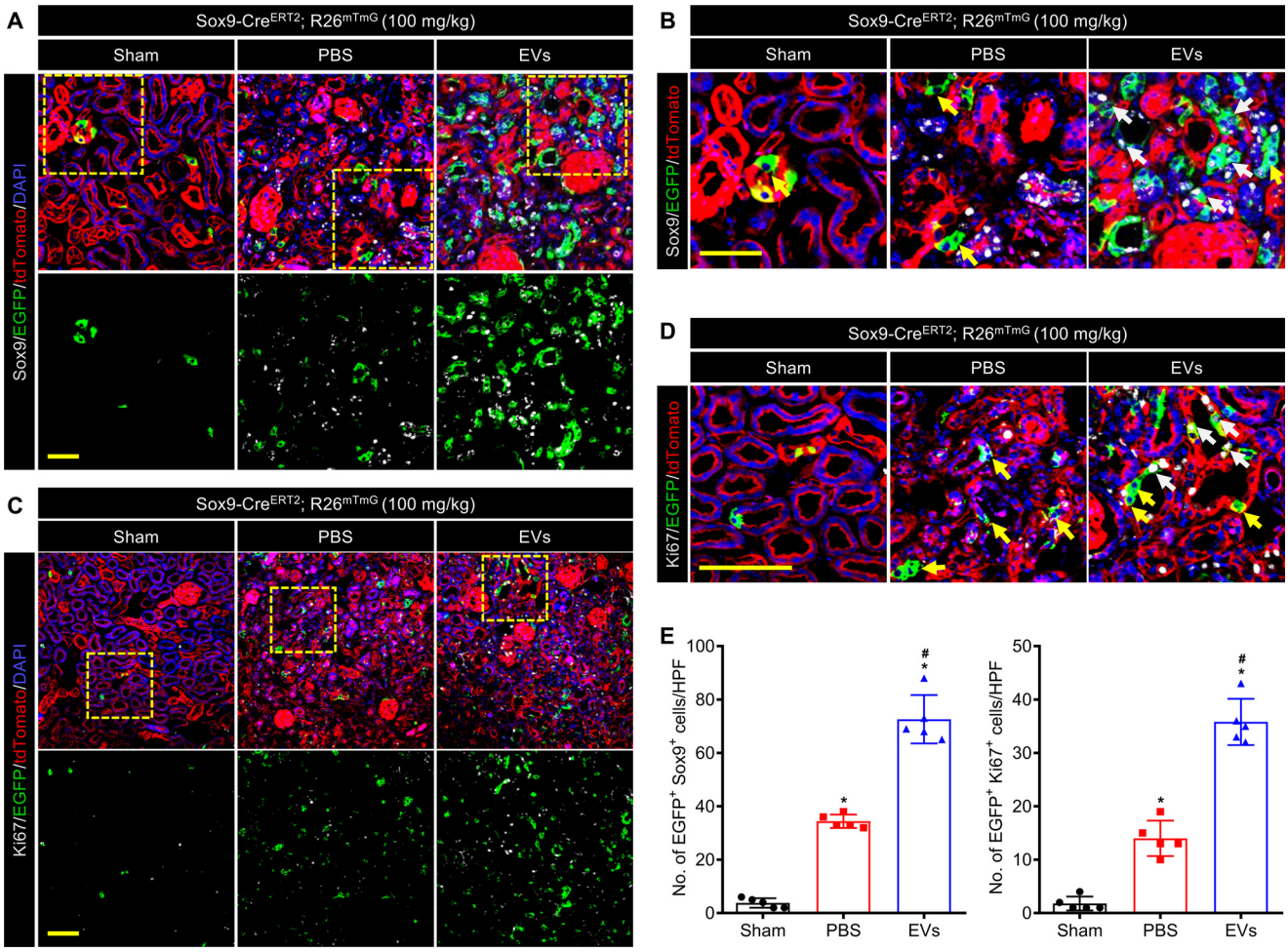


**Figure 6. EVs activated Sox9 expression and Sox9$^+$ cells proliferation during renal regeneration.** *A* and *B*, confocal images (*A*) and local zoom images (*B*) for co-localization analysis of anti-Sox9 immunostaining (*gray*) and Sox9-Cre$^{ERT2}$ activated EGFP fluorescence in kidneys at 14 days post injury. *White arrowheads* highlighted Sox9$^+$/EGFP co-labeled cells, and *yellow arrowheads* highlighted the Sox9$^-$ but EGFP-labeled cells. *Scale bar*, 50 $\mu$M. *C* and *D*, confocal images (*C*) and local zoom images (*D*) for co-localization analysis of anti-Ki67 immunostaining (*gray*) and Sox9-Cre$^{ERT2}$–activated EGFP fluorescence in kidneys at 14 days post injury. *White arrowheads* highlighted Ki67$^+$/EGFP co-labeled cells, and *yellow arrowheads* highlighted the Ki67$^-$ but EGFP-labeled cells. *Scale bar*, 100 $\mu$M. *E*, quantification of Sox9$^+$/EGFP co-labeled cells (*A*) and Ki67$^+$/EGFP co-labeled cells (*C*) in the kidneys of the mice administrated with PBS or EVs on day 14 post IRI. Data are expressed as scatter plots with mean ± S.D. *, $P < 0.05$ *versus* Sham; #, $P < 0.05$ *versus* PBS.

renal repair process in real-time in an individual mouse. Conclusively, our research proposed an effective treatment strategy for AKI and established a practical methodology to study in real-time the development and regeneration of abdominal organs via TPM living imaging through AIW (Fig. 8).

Recent studies have shown that Sox9$^+$ could maintain progenitor-like cell states and the Sox9$^+$ cells could differentiate into proximal tubule, distal tubule, and loop of Henle in the kidney (4, 27). The cell-fate tracing of the descendants of Sox9$^+$ cells revealed that there were very rare Sox9$^+$ cells in the uninjured kidney but a significant increase after injury, which could not be accounted for by expansion of a rare resident Sox9$^+$ population. The dedifferentiation of surviving quiescent renal tubular epithelial cells into a progenitor-like cell state may link to the increase of Sox9$^+$ cells. After AKI, a marked increase of Sox9$^+$ cells with strongly proliferative ability contributed to rapidly replace up to 80% of tubular epithelial cells to ensure the renal regeneration (3). Although the MSC-derived EVs have been reported to improve renal regeneration by increasing the Sox9$^+$ population, the impact of the EVs on resident Sox9$^+$ cells and dedifferentiation of renal tubular epithelial cells was still dimness (10, 14).

Therefore, the development of living imaging strategy, which could in real-time distinguish resident Sox9$^+$ cells *in vivo,* is of great importance to investigate the influence of exogenous therapies on resident Sox9$^+$ cells and their responses in tissue regeneration. In this study, we first confirmed the expansion of resident Sox9$^+$ cells in injured kidney after EV treatment by longitudinal tracking of lineage-labeled Sox9$^+$ cells at cellular resolution through an AIW. Then, we performed anti-Sox9 immunostaining of the injured tissues to investigate the dedifferentiation of surviving tubular epithelial cells. Compared to the significant expansion of EGFP$^+$ cells, the Sox9$^+$/tdTomato$^+$ cells did not discernibly increase in the injured kidney after EV treatment, which illustrated the therapeutic effect of EVs derived from hP-MSCs was relied on promoting expansion of resident Sox9$^+$ cells in AKI treatment.

The Cre-loxP–based lineage tracing, which is increasingly applied to developmental biology and tissue regeneration, provides information about the number, location, and the behavior

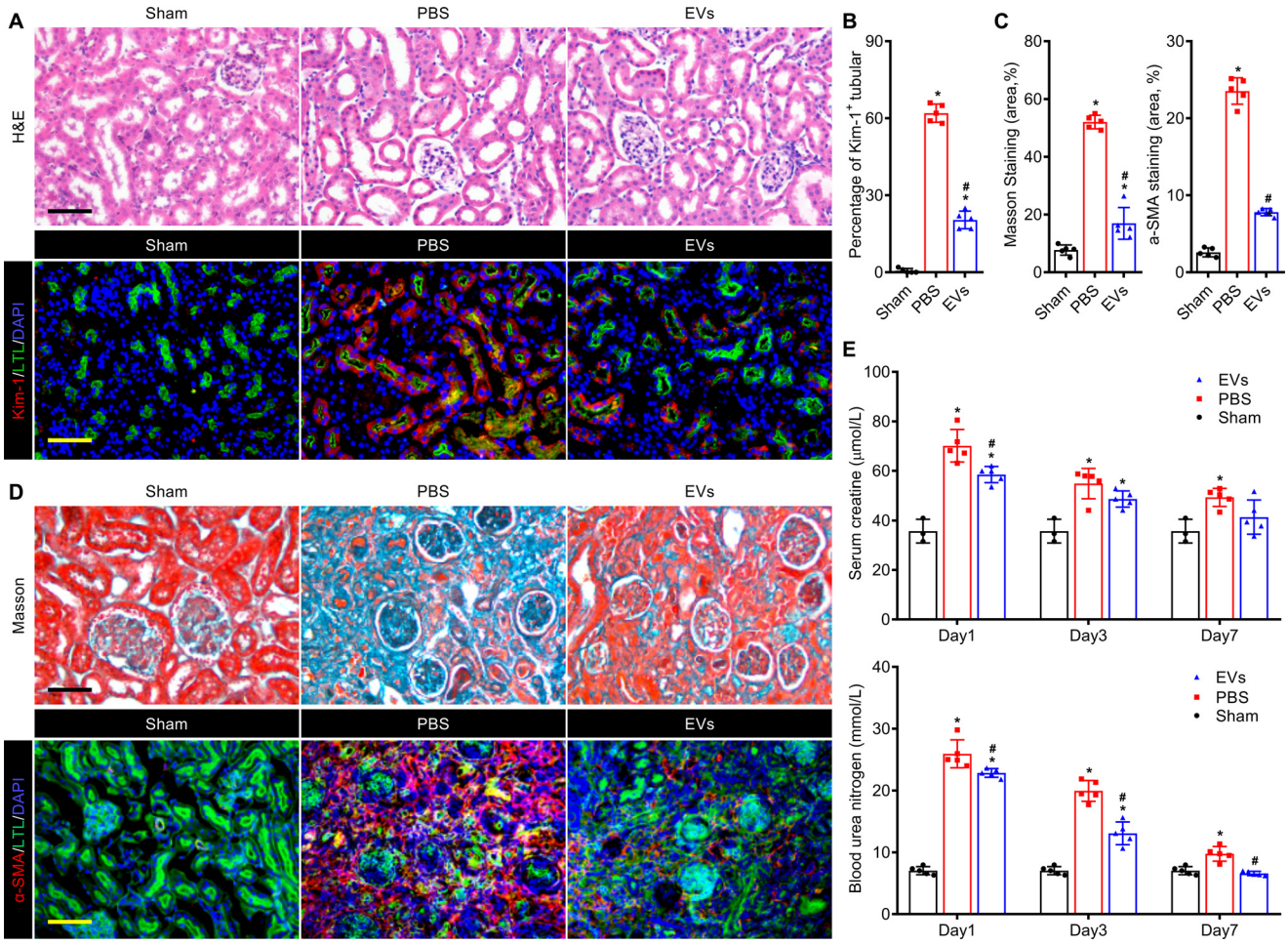


**Figure 7. EVs attenuated renal injury and promoted kidney regeneration in renal IRI mouse model.** *A*, histological analysis of kidney injury by H&E staining and anti–Kim-1 immunostaining (*red*) on day 3 post IRI. The proximal tubules were co-stained by FITC-labeled LTL (*green*). *Scale bar*, 100 μM. *B*, quantitative assessments of Kim-1–positive injured tubules. *C*, quantitative assessments of fibrotic area in Masson staining and anti–α-SMA immunostaining. *D*, representative images of Masson staining and anti–α-SMA immunostaining (*red*) for renal tissues harvested on day 28 post IRI. The proximal tubules were co-stained by FITC-labeled LTL (*green*). *Scale bar*, 100 μM. *E*, serum creatinine and blood urea nitrogen levels of each group were measured on days 1, 3, and 7 post IRI. Data are expressed as scatter plots with mean ± S.D. *, $P < 0.05$ *versus* Sham; #, $P < 0.05$ *versus* PBS.

of the progenies of the founder cell in the intact organism, as opposed to in the states of isolation or *in vitro* culture (19, 28–30). The traditional lineage tracing results which usually are acquired from the fixed and stained tissues sections are only a "snapshot," thus limiting the investigation and interpretation of progenitor cells and their behavior in the pathological and physiological status (31). TPM living imaging through an embedded window, as a promising intravital imaging method to observe deep-tissue in high resolution, has been increasingly used in direct observation of individual cells and 3D reconstruction of organs in the living animals (22, 32).

In previous studies, the TPM living imaging was chiefly performed in the brain where the advantages were convenient fixing and low pigment levels (22, 33, 34). In this study, we applied the very challenging strategy composed of both an imaging window for exposing the organs of interest and TPM living imaging technique for long-term lineage tracing of the abdominal organ in living animals for the first time. This strategy combines the intravital imaging with histopathologic analysis to understand the lineage tracing results, providing a powerful tool to uncover the spatiotemporal dynamics of MSC-derived EVs–induced renal regeneration in high detail.

This strategy, however, has not been widely applied to date in abdominal organs imaging as the motion artifacts caused by breathing and heartbeat of the living animal make image distortions that are hard to compensate for computationally (32). This means the difficulty in successful TPM living imaging of abdominal organs lies not in the hardware or instrumentation but in the ability to fix the living organs sufficiently during imaging. In addition, another difficulty obstructing the large-scale applications of TPM living imaging is the shallow penetration depth because vitrification of the living abdominal solid organs is infeasible (35). To address this problem, a recent study designed an ultradeep TMP with near-IR excitation and emission to accomplish high-resolution bioimaging (36). The near-IR imaging is a superior choice in terms of deep tissue imaging by virtue of the low light–tissue interactions and good penetration capacity of long-wavelength near-IR light, which offers a new idea for lineage tracing imaging of the abdominal solid organs in living animals.

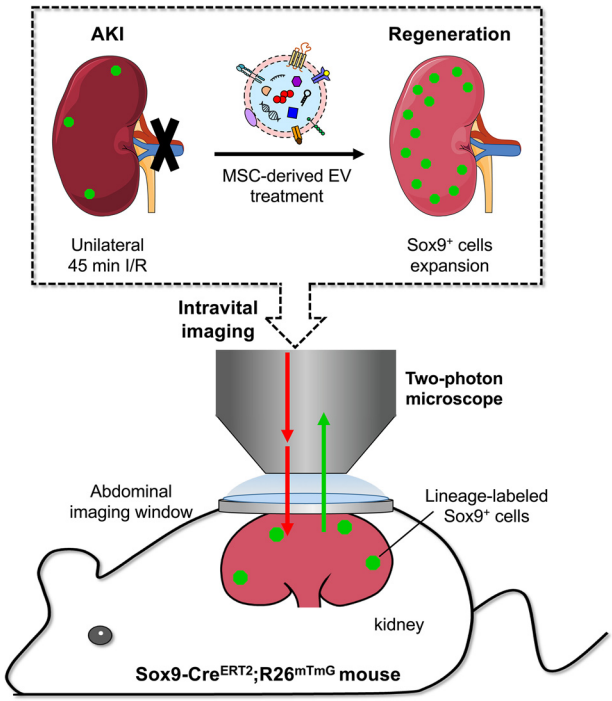


**Figure 8. Schematic diagram of two-photon living imaging of dynamic Sox9-dependent renal regeneration activated by EVs.** Intravital lineage tracing with two-photon intravital microscopy through an abdominal imaging window provides a practical strategy for investigating Sox9-dependent EVs treatment at a high resolution in Sox9-Cre$^{ERT2}$; R26$^{mTmG}$ mouse.

In summary, we investigated the Sox9$^+$ cell–dependent renal regeneration at a high resolution of cellular level after AKI with the treatment of hP-MSC–derived EVs. By using lineage labeling methods and AIW, the longitudinal and temporal evolution of Sox9$^+$ renal cells could be imaged in real-time *in situ* with intravital TMP imaging. Moreover, our results revealed that hP-MSC–derived EVs could ameliorate AKI by promoting the proliferation of Sox9$^+$ cells. Taken together, intravital lineage tracing with TPM through an AIW provides a novel strategy for exploring the kinetic of progenitor cells in tissue regeneration of abdominal organs.

## Experimental Procedures

### *Mice and injury models*

The double-fluorescence Cre reporter mice Rosa26$^{loxP\text{-}mtdTomato\text{-}stop\text{-}loxP\text{–}mEGFP\ (mTmG)}$ and Sox9-Cre$^{ERT2}$ mice were purchased from The Jackson Laboratory (Jax strains 007676 and 018829). Rosa26$^{mTmG}$ mice had the C57BL/6J strain background and Sox9-Cre$^{ERT2}$ mice were a hybrid strain of C57BL/6 and BALB/c. These Rosa26$^{mTmG}$ mice contained a loxP-flanked cell membrane–localized tdTomato (mtdTomato, mT) transgene followed by cell membrane–localized EGFP (mEGFP, mG) in the Rosa26 locus. Prior to Cre recombination, tdTomato fluorescence expression was widespread in cells of the mice. In the Sox9-Cre$^{ERT2}$ mice, Cre$^{ERT2}$ expression was directed by the murine Sox9 promoter and restricted to the cytoplasm. Until exposure to tamoxifen, the Cre$^{ERT2}$ could gain access to the nuclear compartment. In this study, we generated a tamoxifen-inducible mouse line, specifically labeling the Sox9-positive lineage by crossing Sox9-Cre$^{ERT2}$ mice with Rosa26$^{mTmG}$ mice (named as Sox9-Cre$^{ERT2}$; R26$^{mTmG}$ mice). Adult (8–10 weeks, 20–25 g) male mice were employed for all experiments in this study. For induction of Cre$^{ERT2}$ protein, Sox9-Cre$^{ERT2}$; R26$^{mTmG}$ mice were injected with tamoxifen (Sigma-Aldrich, no. T5648) dissolved in corn oil (Sigma-Aldrich, no. C8267), three times (100 mg/kg per day) intraperitoneally, which resulted in Cre$^{ERT2}$-expressing cells. The future cell lineages derived from these cells had EGFP fluorescence expression replacing the tdTomato fluorescence.

The IRI model was established as described previously (37–39). Animals were anesthetized by intraperitoneal injection of 2.5% avertin (Sigma-Aldrich) at a dose of 240 mg/kg, and their eyes were covered with eye-protecting gel (Solcorin, Solco Basie Ltd.). A dorsal longitudinal incision was made to expose the left kidney. Then, the renal pedicle was clamped with a non-traumatic microvascular clamp for 45 min. The clamp was removed to induce blood reperfusion after the period of ischemia had concluded. Reperfusion was confirmed visually before the incision was closed. As for mice used in intravital imaging, the AIW was implanted as described previously (23, 40). The AIW consisted of a reusable titanium ring with a groove on the side and a coverslip on the top. The sterile AIW was tightly secured on the skin and abdominal wall within the groove of the ring using a purse-string suture, which ensured that there was no direct opening to the abdomen. Then the mice received three consecutive intravenous injections of EVs at a dose of 100 $\mu$g in a volume of 100 $\mu$l per day. The treatment of animals and the experimental procedures of the present study adhere to the Nankai University Animal Care and Use Committee Guidelines that conform to the Guidelines for Animal Care approved by the National Institutes of Health (NIH).

### *Fluorescence stereomicroscope imaging and two-photon imaging in living mice*

We used a fluorescence stereomicroscope system from Nikon (AZ100; Nikon Co., Tokyo, Japan) and a two-photon microscope system from Olympus (FV1000; Olympus, Tokyo, Japan). All imaging experiments were performed in a dark and nonvibrating environment. An AIW was implanted in the abdomen of the mouse which was fixed with an adapter and maintained under anesthesia by injecting avertin. The objective lens was 25× and was immersed in water on the AIW window in the mouse abdomen. The two-photon excitation was performed at a wavelength of 835 nm (10% laser transmissivity), and the emission was collected at 495–540 nm (EGFP) and 575–630 nm (tdTomato) (Fig. S10). Scanning was advanced with Z-steps of 5 $\mu$M, a 1 zoom under the 25× objective lens (580 $\mu$M × 580 $\mu$M single scanning area) and an 800 × 800 pixel size.

### *Renal function analysis*

For the renal function analysis, unilateral (left) 45-min ischemia/reperfusion injury plus contralateral nephrectomy was performed on the animals. On days 1, 3, and 7 post injury, blood samples were harvested from orbit and the sera were collected for renal function analysis. The concentrations of blood urea

nitrogen (BUN) and serum creatinine (SCr) were measured by using the BUN assay kit (Nanjing Jiancheng Bioengineering Institute, Nanjing, China) and the SCr assay kit (Nanjing Jiancheng Bioengineering Institute), respectively.

### *Histological analysis of renal tissue*

At indicated time points, the animals were euthanized to harvest the kidney samples. For paraffin sections, the kidney samples were fixed with 4% paraformaldehyde, dehydrated with ethyl alcohol, hyalinized with xylene, and eventually embedded in paraffin (Leica Microsystems, Wetzlar, Germany). For cryosection, the kidney samples were fixed with 4% paraformaldehyde, dehydrated with 30% sucrose solution, and embedded into Optimal Cutting Temperature Compound (Sakura Finetek, Tokyo, Japan). All the samples were cut into a series of sections of 5 $\mu$M in thickness. The H&E staining and Masson staining were performed on paraffin sections according to a standard protocol, whereas frozen sections were used for immunofluorescent staining.

For immunostaining, the cryosections were incubated with a series of primary antibodies: anti-Sox9 (1:200; Cell Signaling Technology), anti-PCNA (1:200; Abcam), anti-Ki67 (1:200; Abcam), anti-E-cadherin (1:200; Abcam), anti-Kim-1 (1:200; Abcam), and anti-$\alpha$-SMA (1:200; Abcam) overnight at 4°C. Then, the Alexa Fluor 488–, Alexa Fluor 594–, and Alexa Fluor 647–labeled goat anti-rabbit or goat anti-mouse antibodies (1:400; Life Technologies) were used for the immunofluorescence staining. The FITC-labeled Lotus tetragonolobus lectin (LTL, 1:400, Vector Laboratories, Burlingame, CA) and rhodamine-labeled lens culinaris agglutinin (LCA, 1:400, Vector Laboratories) were used to disclose renal structure, and 4′-6-diamidino-2-phenylindole (DAPI) (1:500, Vector Laboratories) was used to visualize the nucleus. The quantitative analysis of the immunostaining was measured by ImageJ software.

### *Statistical analysis*

All results presented are from at least three independent experiments for each condition. Data are expressed as scatter plots with mean ± S.D. Statistical analysis was performed by one- or two-way analysis of variance using GraphPad (PRISM software). Differences were considered statistically significant at $p < 0.05$.

## Data availability

All data are contained within the article.

*Author contributions*—K. Z., Z.-C. H., G. Z., and Z. L. conceptualization; K. Z. and S. C. data curation; K. Z., S. C., and Z. L. formal analysis; K. Z., S. C., H. S., L. W., Z. G., G. Z., X. C., and Z. L. investigation; K. Z., S. C., H. S., L. W., H. L., J. Z., C. Z., Z. H., and Z. L. methodology; K. Z., S. C., G. Z., and Z. L. writing-original draft; K. Z., S. C., Z.-C. H., G. Z., X. C., and Z. L. writing-review and editing; S. C., N. L., Z. G., Z. H., G. Z., and X. C. resources; S. C. software; N. L., Z. G., and Z. L. project administration; Z. H., Z.-C. H., X. C., and Z. L. supervision; G. Z. validation; X. C. and Z. L. funding acquisition; Z. L. visualization.

*Funding and additional information*—This research was supported by the National Key R&D Program of China Grant 2017YFA0103200 (to Z. L.), National Natural Science Foundation of China Grant 81671734 (to Z. L.).

*Conflict of interest*—The authors declare that they have no conflicts of interest with the contents of this article.

*Abbreviations*—The abbreviations used are: AIW, abdominal imaging window; AKI, acute kidney injury; BLI, bioluminescence imaging; BUN, blood urea nitrogen; DAPI, 4′-6-diamidino-2-phenylindole; EV, extracellular vesicle; Gluc, Gaussia luciferase; hP-MSC, human placenta–derived MSCs; IRI, ischemia-reperfusion injury; LCA, lens culinaris agglutinin; LTL, Lotus tetragonolobus lectin; MSC, mesenchymal stem cell; PCNA, proliferating cell nuclear antigen; SCr, serum creatinine; TEC, tubule epithelial cell; TPM, two-photon microscopy; $\alpha$-SMA, $\alpha$-smooth muscle actin.

## References

1. Lameire, N. H., Bagga, A., Cruz, D., De Maeseneer, J., Endre, Z., Kellum, J. A., Liu, K. D., Mehta, R. L., Pannu, N., Van Biesen, W., and Vanholder, R. (2013) Acute kidney injury: An increasing global concern. *Lancet* **382,** 170–179 CrossRef Medline
2. Hoste, E. A. J., Kellum, J. A., Selby, N. M., Zarbock, A., Palevsky, P. M., Bagshaw, S. M., Goldstein, S. L., Cerdá, J., and Chawla, L. S. (2018) Global epidemiology and outcomes of acute kidney injury. *Nat. Rev. Nephrol.* **14,** 607–625 CrossRef Medline
3. Kumar, S., Liu, J., Pang, P., Krautzberger, A. M., Reginensi, A., Akiyama, H., Schedl, A., Humphreys, B. D., and McMahon, A. P. (2015) Sox9 activation highlights a cellular pathway of renal repair in the acutely injured mammalian kidney. *Cell Rep.* **12,** 1325–1338 CrossRef Medline
4. Kang, H. M., Huang, S., Reidy, K., Han, S. H., Chinga, F., and Susztak, K. (2016) Sox9-positive progenitor cells play a key role in renal tubule epithelial regeneration in mice. *Cell Rep.* **14,** 861–871 CrossRef Medline
5. Agrahari, V., Agrahari, V., Burnouf, P. A., Chew, C. H., and Burnouf, T. (2019) Extracellular microvesicles as new industrial therapeutic frontiers. *Trends Biotechnol.* **37,** 707–729 CrossRef Medline
6. Pegtel, D. M., and Gould, S. J. (2019) Exosomes. *Annu. Rev. Biochem.* **88,** 487–514 CrossRef Medline
7. Lv, K., Li, Q., Zhang, L., Wang, Y., Zhong, Z., Zhao, J., Lin, X., Wang, J., Zhu, K., Xiao, C., Ke, C., Zhong, S., Wu, X., Chen, J., Yu, H., *et al.* (2019) Incorporation of small extracellular vesicles in sodium alginate hydrogel as a novel therapeutic strategy for myocardial infarction. *Theranostics* **9,** 7403–7416 CrossRef Medline
8. Du, W., Zhang, K., Zhang, S., Wang, R., Nie, Y., Tao, H., Han, Z., Liang, L., Wang, D., Liu, J., Liu, N., Han, Z., Kong, D., Zhao, Q., and Li, Z. (2017) Enhanced proangiogenic potential of mesenchymal stem cell-derived exosomes stimulated by a nitric oxide releasing polymer. *Biomaterials* **133,** 70–81 CrossRef Medline
9. Wei, Y., Wu, Y., Zhao, R., Zhang, K., Midgley, A. C., Kong, D., Li, Z., and Zhao, Q. (2019) MSC-derived sEVs enhance patency and inhibit calcification of synthetic vascular grafts by immunomodulation in a rat model of hyperlipidemia. *Biomaterials* **204,** 13–24 CrossRef Medline
10. Bian, X., Ma, K., Zhang, C., and Fu, X. (2019) Therapeutic angiogenesis using stem cell-derived extracellular vesicles: An emerging approach for treatment of ischemic diseases. *Stem Cell Res. Ther.* **10,** 158 CrossRef Medline
11. Wiklander, O. P. B., Brennan, M. A., Lötvall, J., Breakefield, X. O., and El Andaloussi, S. (2019) Advances in therapeutic applications of extracellular vesicles. *Sci. Transl. Med.* **11,** eaav8521 CrossRef Medline
12. Tao, H., Chen, X., Cao, H., Zheng, L., Li, Q., Zhang, K., Han, Z., Han, Z. C., Guo, Z., Li, Z., and Wang, L. (2019) Mesenchymal stem cell-derived extracellular vesicles for corneal wound repair. *Stem Cells Int.* **2019,** 5738510 CrossRef Medline

13. Liao, Z., Luo, R., Li, G., Song, Y., Zhan, S., Zhao, K., Hua, W., Zhang, Y., Wu, X., and Yang, C. (2019) Exosomes from mesenchymal stem cells modulate endoplasmic reticulum stress to protect against nucleus pulposus cell death and ameliorate intervertebral disc degeneration *in vivo*. *Theranostics* **9,** 4084–4100 CrossRef Medline
14. Aghajani Nargesi, A., Lerman, L. O., and Eirin, A. (2017) Mesenchymal stem cell-derived extracellular vesicles for kidney repair: Current status and looming challenges. *Stem Cell Res. Ther.* **8,** 273 CrossRef Medline
15. Zhang, A., Wang, H., Wang, B., Yuan, Y., Klein, J. D., and Wang, X. H. (2019) Exogenous mir-26a suppresses muscle wasting and renal fibrosis in obstructive kidney disease. *FASEB J.* **33,** 13590–13601 CrossRef Medline
16. Shi, J., Duan, J., Gong, H., Pang, Y., Wang, L., and Yan, Y. (2019) Exosomes from mir-20b-3p-overexpressing stromal cells ameliorate calcium oxalate deposition in rat kidney. *J. Cell. Mol. Med.* **23,** 7268–7278 CrossRef Medline
17. Zhu, F., Chong Lee Shin, O. L. S., Pei, G., Hu, Z., Yang, J., Zhu, H., Wang, M., Mou, J., Sun, J., Wang, Y., Yang, Q., Zhao, Z., Xu, H., Gao, H., Yao, W., *et al.* (2017) Adipose-derived mesenchymal stem cells employed exosomes to attenuate AKI-CKD transition through tubular epithelial cell dependent sox9 activation. *Oncotarget* **8,** 70707–70726 CrossRef Medline
18. Chari, S., Nguyen, A., Saxe, J., and Sweet, D. J. (2017) Lineage tracing across 10 years. *Cell Stem Cell* **20,** 733–734 CrossRef Medline
19. Spanjaard, B., and Junker, J. P. (2017) Methods for lineage tracing on the organism-wide level. *Curr. Opin. Cell Biol.* **49,** 16–21 CrossRef Medline
20. Kester, L., and van Oudenaarden, A. (2018) Single-cell transcriptomics meets lineage tracing. *Cell Stem Cell* **23,** 166–179 CrossRef Medline
21. Ma, Q., Wang, Y., Zhang, T., and Zuo, W. (2018) Notch-mediated sox9$^+$ cell activation contributes to kidney repair after partial nephrectomy. *Life Sci.* **193,** 104–109 CrossRef Medline
22. Zong, W., Wu, R., Li, M., Hu, Y., Li, Y., Li, J., Rong, H., Wu, H., Xu, Y., Lu, Y., Jia, H., Fan, M., Zhou, Z., Zhang, Y., Wang, A., *et al.* (2017) Fast high-resolution miniature two-photon microscopy for brain imaging in freely behaving mice. *Nat. Methods* **14,** 713–719 CrossRef Medline
23. Ritsma, L., Steller, E. J., Beerling, E., Loomans, C. J., Zomer, A., Gerlach, C., Vrisekoop, N., Seinstra, D., van Gurp, L., Schäfer, R., Raats, D. A., de Graaff, A., Schumacher, T. N., de Koning, E. J., Rinkes, I. H., *et al.* (2012) Intravital microscopy through an abdominal imaging window reveals a pre-micrometastasis stage during liver metastasis. *Sci. Transl. Med.* **4,** 158ra145 CrossRef Medline
24. Alieva, M., Ritsma, L., Giedt, R. J., Weissleder, R., and van Rheenen, J. (2014) Imaging windows for long-term intravital imaging: General overview and technical insights. *Intravital* **3,** e29917 CrossRef Medline
25. Revell, D. Z., and Yoder, B. K. (2019) Intravital visualization of the primary cilium, tubule flow, and innate immune cells in the kidney utilizing an abdominal window imaging approach. *Methods Cell Biol.* **154,** 67–83 CrossRef Medline
26. Zhang, K., Zhao, X., Chen, X., Wei, Y., Du, W., Wang, Y., Liu, L., Zhao, W., Han, Z., Kong, D., Zhao, Q., Guo, Z., Han, Z., Liu, N., Ma, F., *et al.* (2018) Enhanced therapeutic effects of mesenchymal stem cell-derived exosomes with an injectable hydrogel for hindlimb ischemia treatment. *ACS Appl. Mater. Interfaces* **10,** 30081–30091 CrossRef Medline
27. Kumar, S. (2018) Cellular and molecular pathways of renal repair after acute kidney injury. *Kidney Int.* **93,** 27–40 CrossRef Medline
28. Kretzschmar, K., and Watt, F. M. (2012) Lineage tracing. *Cell* **148,** 33–45 CrossRef Medline
29. Zhang, Y., Xu, J., Liu, S., Lim, M., Zhao, S., Cui, K., Zhang, K., Wang, L., Ji, Q., Han, Z., Kong, D., Li, Z., and Liu, N. (2019) Embryonic stem cell-derived extracellular vesicles enhance the therapeutic effect of mesenchymal stem cells. *Theranostics* **9,** 6976–6990 CrossRef Medline
30. Lloyd-Lewis, B., Harris, O. B., Watson, C. J., and Davis, F. M. (2017) Mammary stem cells: Premise, properties, and perspectives. *Trends Cell Biol.* **27,** 556–567 CrossRef Medline
31. Romagnani, P., Rinkevich, Y., and Dekel, B. (2015) The use of lineage tracing to study kidney injury and regeneration. *Nat. Rev. Nephrol.* **11,** 420–431 CrossRef Medline
32. Entenberg, D., Pastoriza, J. M., Oktay, M. H., Voiculescu, S., Wang, Y., Sosa, M. S., Aguirre-Ghiso, J., and Condeelis, J. (2017) Time-lapsed, large-volume, high-resolution intravital imaging for tissue-wide analysis of single cell dynamics. *Methods* **128,** 65–77 CrossRef Medline
33. Heo, C., Park, H., Kim, Y. T., Baeg, E., Kim, Y. H., Kim, S. G., and Suh, M. (2016) A soft, transparent, freely accessible cranial window for chronic imaging and electrophysiology. *Sci. Rep.* **6,** 27818 CrossRef Medline
34. Hillman, E. M. (2007) Optical brain imaging *in vivo*: Techniques and applications from animal to man. *J. Biomed. Opt.* **12,** 051402 CrossRef Medline
35. Kaufmann, R., Hagen, C., and Grünewald, K. (2014) Fluorescence cryo-microscopy: Current challenges and prospects. *Curr. Opin. Chem. Biol.* **20,** 86–91 CrossRef Medline
36. Qi, J., Sun, C., Li, D., Zhang, H., Yu, W., Zebibula, A., Lam, J. W. Y., Xi, W., Zhu, L., Cai, F., Wei, P., Zhu, C., Kwok, R. T. K., Streich, L. L., Prevedel, R., *et al.* (2018) Aggregation-induced emission luminogen with near-infrared-II excitation and near-infrared-I emission for ultradeep intravital two-photon microscopy. *ACS Nano.* **12,** 7936–7945 CrossRef Medline
37. Feng, G., Zhang, J., Li, Y., Nie, Y., Zhu, D., Wang, R., Liu, J., Gao, J., Liu, N., He, N., Du, W., Tao, H., Che, Y., Xu, Y., Kong, D., *et al.* (2016) IGF-1 C domain-modified hydrogel enhances cell therapy for AKI. *J. Am. Soc. Nephrol.* **27,** 2357–2369 CrossRef Medline
38. Liu, Y., Cui, J., Wang, H., Hezam, K., Zhao, X., Huang, H., Chen, S., Han, Z., Han, Z. C., Guo, Z., and Li, Z. (2020) Enhanced therapeutic effects of MSC-derived extracellular vesicles with an injectable collagen matrix for experimental acute kidney injury treatment. *Stem Cell Res. Ther.* **11,** 161 CrossRef Medline
39. Feng, G., Mao, D., Che, Y., Su, W., Wang, Y., Xu, Y., Fan, Y., Zhao, H., Kong, D., Xu, Y., and Li, Z. (2013) The phenotypic fate of bone marrow-derived stem cells in acute kidney injury. *Cell Physiol. Biochem.* **32,** 1517–1527 CrossRef Medline
40. Ritsma, L., Steller, E. J., Ellenbroek, S. I., Kranenburg, O., Borel Rinkes, I. H., and van Rheenen, J. (2013) Surgical implantation of an abdominal imaging window for intravital microscopy. *Nat. Protoc.* **8,** 583–594 CrossRef Medline